Supplementary Information for: Structures, Thermodynamics and Dynamics of Topological Defects in Gay–Berne Nematic Liquid Crystals

Yulu Huang[a], Weiqiang Wang[a], Jonathan K. Whitmer[b] and Rui Zhang[a*]

[a] *Department of Physics, The Hong Kong University of Science and Technology, Clear Water Bay, Kowloon, Hong Kong, P.R. China*

[b] *Department of Chemical and Biomolecular Engineering, University of Notre Dame, Notre Dame, IN 46556, USA*

1 Potential

Three Gay–Berne (GB) models are studied in this work, and their corresponding potentials are shown in Fig. S.1.
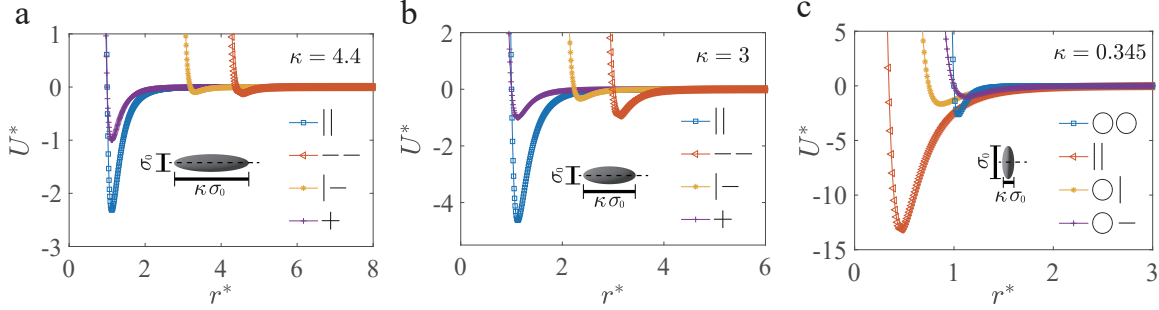

Figure S.1. Gay–Berne potential corresponding to $GB(4.4, 20, 1, 1)$ (a), $GB(3, 5, 1, 3)$ (b) and $GB(0.345, 0.2, 1, 2)$ (c). Insets: characteristic dimensions of the GB particle, dashed black lines indicate the uni-axis of the particles. σ_0 is the diameter of the cross-section of the particle normal to its orientation, κ represents the aspect ratio of the GB particle.

2 Size effect of sampling region

When analyzing the MD simulation results in the main text, we divided the simulation box into grids in the xy plane and measured the scalar order parameter and director in each grid (sampling) region. The number of GB particles in the individual grid region is denoted by N^{r}. The **Q** tensor defined in the main text can be diagonalized and the alignment tensor can be written as follows:

$$Q = \begin{pmatrix} \frac{2S}{3} & 0 & 0 \\ 0 & -\frac{S+P}{3} & 0 \\ 0 & 0 & -\frac{S-P}{3} \end{pmatrix},$$

where S is the scalar order parameter and P is the biaxiality.

Here we study the size effect of the sampling region on the scalar order parameter S_{bulk} and biaxiality P_{bulk}. As shown in Fig. S.2a, we find the bulk scalar order parameter S_{bulk} is only

marginally dependent on N^{r}, and its fluctuation decreases as N^{r} increases. The bulk biaxiality P_{bulk} is, however, dependent on the sampling region size N^{r}, with its value approaches to zero with the increase of N^{r} (Fig. S.2b). When N^{r} is not sufficiently large, the biaxiality is nonzero. $N^{\mathrm{r}} > 500$ is required to minimize such size effect.
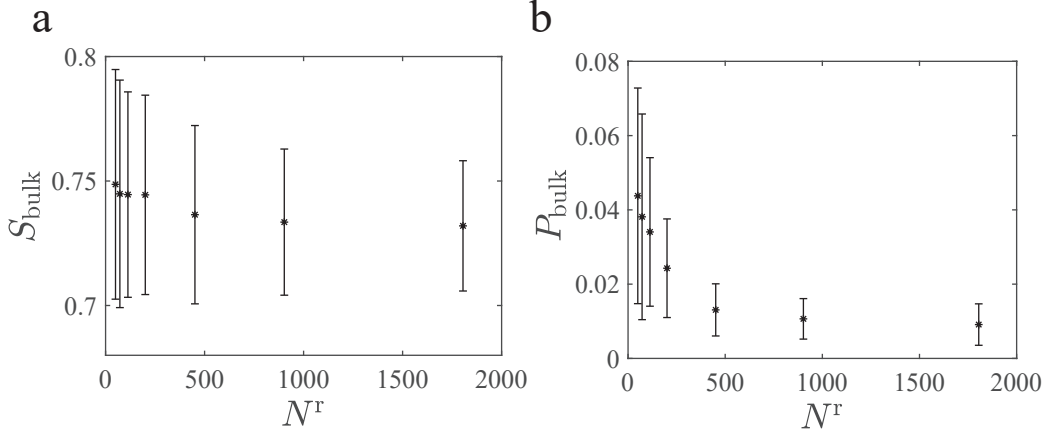
a b

Figure S.2. Bulk scalar order parameters (a) and bulk biaxiality (b) as a function of the number in one window. Error bars indicate standard deviation of 10 measurements.

3   Defect core

We measured the spatial profiles of the scalar order parameter S and biaxiality P in Fig. S.3, from which we observe that defect cores are heavily biaxial, consistent with literature.[5] We notice that the measurement of the local biaxiality depends on the sampling region size (Size effect section), which approaches to zero with the increase of the number of GB particles in the individual grid region N^{r} (Fig. S.2b). Due to the limitation of the system size, $N^{\mathrm{r}} \sim 50$ in our measurement, leading to non-zero biaxiality in the bulk region $r^* > 15$.
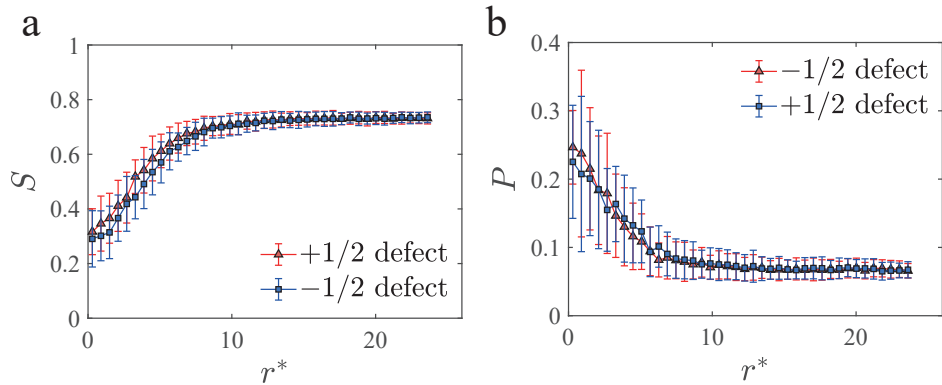
Figure S.3. Scalar order parameters (a) and biaxiality (b) as a function of distance from the defect center. Error bars indicate standard deviation of 100 measurements.

The **Q**-tensor eigenvalues of defect cores are plotted in Fig. S.4, showing the same trend as the literature when away from the defect core.[5] Our simulation indicates that the defect core is still (positively) uniaxial, with its **Q**-tensor having one positive and two negative eigenvalues. This is different from the predication by the literature that the defect core is strongly biaxial, with its core center having two positive and one negative eigenvalues for its **Q**-tensor.[5]
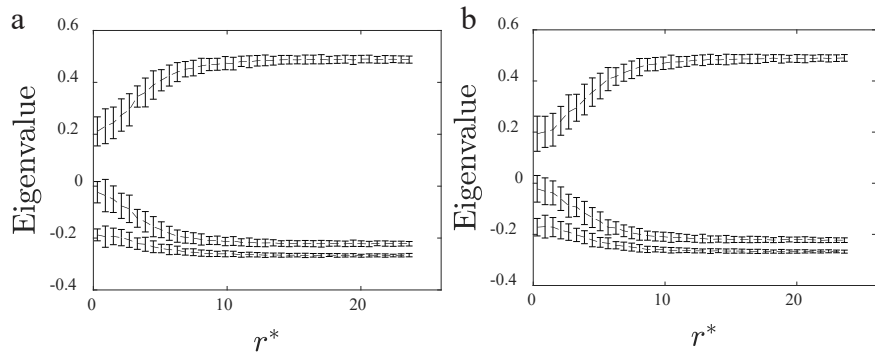

Figure S.4. Eigenvalues of **Q**-tensor as a function of distance from the defect center of $+1/2$ (a) and $-1/2$ (b) defect. Error bars indicate standard deviation of 100 measurements.

To further investigate the fine structure of defect cores, we also plot the energy distribution near defect cores in Fig. S.5. We did find that the total energy (kinetic plus potential energy) shows non-monotonic behavior with respect to the distance from a $-1/2$ defect core, which is consistent with the literature.[5] Interestingly, the potential energy profile near a $+1/2$ defect core
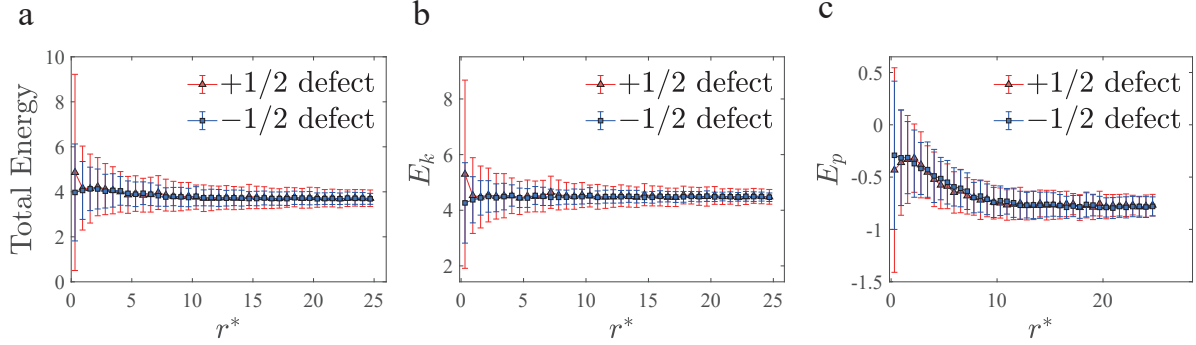
Figure S.5. Energy distribution near the defect core. (a) Total energy distribution. (b) Kinetic energy distribution. (c) Potential energy distribution. Error bars indicate standard deviation of 100 measurements.

also shows a dip at the core. However, there are significant fluctuations in the kinetic energy data for $+1/2$ defects and we cannot draw an affirmative conclusion.

The above differences between MD simulations and continuum theory predictions can be understood by a temperature effect. As discussed in Ref.[5], defect core becomes large in size and exhibits domain-wall-like structure at a temperature close to T_{NI} (temperature scale $\bar{A} = 0.25$ leading to $S_{\mathrm{bulk}} \sim 0.443$); in a low temperature at which defect core becomes smaller, the domain-wall-like core structure will be replaced by a single peak structure (temperature scale $\bar{A} = -1$ and $S_{\mathrm{bulk}} \sim 0.729$).[5] The disappearance of the crater-like (or domain-wall-like) structure for the defect cores in our molecular simulations is consistent with the fact that the scalar order parameter in our simulation is high, i.e., $S \sim 0.7$. The high scalar order parameter of the bulk nematic and the smallness of the defect core in our simulations prevent us from observing the domain-wall-like structure and the negative uniaxiality at defect core centers. Extensive simulations with wider temperature range will be conducted in future works to ascertain these features predicted by the continuum theory.

4 Continuum model

The continuum simulation is based on the Landau–de Gennes free energy functional[1,6] in terms of the tensorial order parameter $\mathbf{Q}$, which is linked to the unit vector $\hat{\mathbf{n}}$ of the director field through $\mathbf{Q} = \langle \hat{\mathbf{n}}\hat{\mathbf{n}} - \mathbf{I}/3 \rangle$, with $\langle \cdot \rangle$ being the ensemble average. The bulk free energy $\mathcal{F}$ of

5

the nematic is given as

$$\mathcal{F} = \int_V (f_{\text{LdG}} + f_{\text{el}})dV,$$ (S.1)

where f_{LdG} is the Landau-de Gennes free energy and f_{el} is the elastic energy. f_{LdG} takes the following form[1]

$$f_{\text{LdG}} = \frac{A_0}{2}\left(1 - \frac{U}{3}\right)\text{Tr}(\mathbf{Q}^2) - \frac{A_0 U}{3}\text{Tr}(\mathbf{Q}^3) + \frac{A_0 U}{4}\text{Tr}(\mathbf{Q}^2)^2,$$

where parameter A_0, and U controls the magnitude of S of a homogeneous static system through

$$S = \frac{1}{4} + \frac{3}{4}\sqrt{1 - \frac{8}{3U}}.$$

The elastic energy density f_{el} in the simulation is expressed in terms of $\mathbf{Q}$-tensor form as

$$f_{\text{el}} = \frac{1}{2}L_1(\partial_k Q_{ij})(\partial_k Q_{ij}) + \frac{1}{2}L_2(\partial_k Q_{jk})(\partial_l Q_{jl})$$
$$+ \frac{1}{2}L_3 Q_{ij}(\partial_i Q_{kl})(\partial_j Q_{kl}) + \frac{1}{2}L_4(\partial_l Q_{jk})(\partial_k Q_{jl}).$$

The mapping between constant sets K_1, K_2, K_3, K_{24} and L_1, L_2, L_3, L_4 is

$$L_1 = \frac{1}{2S^2}[K_2 + \frac{1}{3}(K_3 - K_1)],$$
$$L_2 = \frac{1}{S^2}(K_1 - K_{24}),$$
$$L_3 = \frac{1}{2S^3}(K_3 - K_1),$$
$$L_4 = \frac{1}{S^2}(K_{24} - K_2).$$

To minimize the free energy in Eq. S.1, we introduce the molecular field,

$$\mathbf{H} = -\left[\frac{\delta \mathcal{F}}{\delta \mathbf{Q}}\right]^{\text{st}},$$

where $[...]^{\text{st}}$ is a symmetric and traceless operator. The evolution of the bulk points is governed by

$$\partial_t \mathbf{Q} = \Gamma_s \mathbf{H},$$

where Γ_s is the relaxation constant and t is simulation time. In the disk simulation, a fixed homeotropic anchoring condition is adopted.

6

5 Size effect in disk system

In the disk system, we measured the distance between two $+1/2$ defects in the nematic confined to a disk region ($D^* = 21.04 - 176$) with homeotropic anchoring to infer the ratio of splay and bend constant. The scalar order parameter $S \sim S_{\text{bulk}}$ is adopted in all simulations, where S_{bulk} is the bulk scalar order parameter parameter shown in the main text Table. 2. The results, summarized in Fig. 2b (main text), show that the agreement between MD simulation and theory is not sensitive to the choice of disk size.

We discuss two main possible contribution factors to the inaccuracy of this method. Finite anchoring effect of the disk boundary can lead to over-estimated d/D in the simulation. The two $+1/2$ defects are elastically repelling each other; they are confined within the disk through a repulsive force by the boundary. In the MD simulation, we used a fixed layer of GB particles to generate the homeotropic anchoring. The density ratio n_ρ between boundary particles and bulk particles is chosen to be 1 for prolate particles ($\kappa = 4.4$ and 3), and 3.7 for oblate particles ($\kappa = 0.345$). This density ratio sets the anchoring strength by setting the ratio between nematic-wall interaction U_{WN} and nematic-nematic interaction U. The extrapolation length $b = K/W$ with K being the elastic constant and W being the anchoring strength, can be estimated according to[1]

$$b \sim a\frac{U}{U_{\text{WN}}} \sim \frac{\kappa}{n_\rho}(\text{prolate}),$$

$$b \sim a\frac{U}{U_{\text{WN}}} \sim \frac{1}{n_\rho}(\text{oblate}),$$

where a represents an average molecular dimension. The theory is based on the infinite anchoring assumption, which corresponds to $\frac{b}{D} = 0$. When the anchoring strength is finite ($0.05 < \frac{b}{D} < 0.1$), as is the case in the simulation, the boundary repulsion force is weakened, and the two elastically repelling defects will move farther from each other, rendering d/D larger than the theoretical value.

Another factor is the unevenly distributed scalar order parameter in the disk, which can lead to under-estimated d/D in the MD simulation. The scalar order parameter is low near defect core and high near the confinement. When disk size is small, defect regions become relatively important. The lowering of the scalar order parameter in the neighborhood region of the defects

can soften the elastic modulus, and therefore weakens the repulsion force between them. On the other hand, the enhancement of the scalar order parameter near boundary can increase the repulsive force of the defect by the boundary. These two mechanisms can lead to lower d/D. This effect can be ignored when $\frac{b}{D} \ll 1$ and $\frac{r_c}{D} \ll 1$.

6   Annihilation event with a small size

To further investigate the size effect on the annihilation, we plot defect trajectories in a smaller system ($d^* \sim 30$) shown in Fig. S.6.
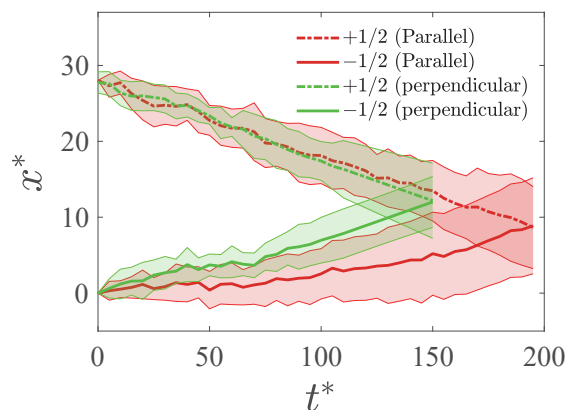

Figure S.6. Defects position in x-axis as a function of time ($d^* \sim 30$), error bars indicate standard deviation of 10 independent simulation runs.

These trajectories appear similar to the later-stage trajectories in the larger system (Fig. 3c in main text). No significant size effect is observed in the above size range. For even smaller system, defect annihilation occurs too fast and measurement becomes difficult.

7   Rotational viscosity of the Gay–Berne model

7.1   Measurement of rotational viscosity in MD simulation

To estimate the Ericksen number of the nematic GB system, we use a rotating field method to measure the rotational viscosity of the GB$(4.4, 20, 1, 1)$ model.[2]

In the simulation, the initial configuration is a uniform nematic with its director aligned along the x-axis. We applied an external field (electric or magnetic) to force the GB particles to rotate, the artificial force potential can be defined as follows:

$$U_{\text{arti}} = -\sum_{i=1}^{N} (\hat{\mathbf{u}}_i \cdot \mathbf{a})^2 / \mid \mathbf{a} \mid,$$

where $\mathbf{a}$ is a constant vector representing the artificial external field. We define β as the angle between the director and the artificial field $\mathbf{a}$.
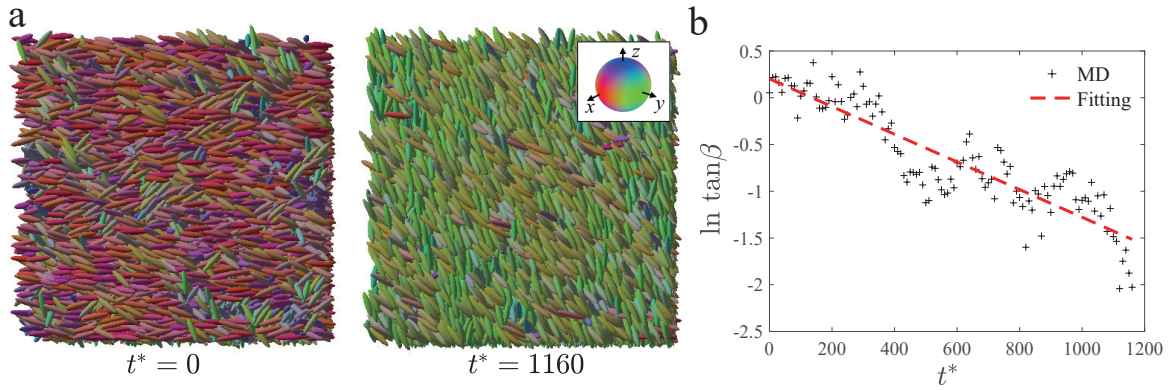

Figure S.7. Measurement of rotational viscosity. (a) Snapshots of the field-aligned simulation at the start of the director rotation and $t^* = 1160$ later. (b) Variation of the director angle β with time t.

To extract the rotational viscosity of the system, we measure the time evolution of the director rotation following the relation between the torque M and the angular velocity $\dot{\beta}$:

$$M/V = -\gamma_1^* \dot{\beta}, \tag{S.2}$$

where γ_1^* is the rotational viscosity. The summation of each molecular torque vector $\mathbf{M}$ can be written as:

$$\mathbf{M} = \frac{2}{\mid \mathbf{a} \mid} \sum_{i=1}^{N} (\hat{\mathbf{u}}_i \cdot \mathbf{a}) (\hat{\mathbf{u}}_i \times \mathbf{a}).$$

The system is in the nematic phase, we assume that the system is fully uniaxial at any moment. The above equation can be rewritten as:

$$M = 2N \mid \mathbf{a} \mid S \sin\beta \cos\beta. \tag{S.3}$$

Combining Equation S.2 and S.3, we obtain a simple differential equation:

$$\ln \tan \beta = -\frac{2N|\mathbf{a}|S}{\gamma_1^* V} t + C,$$

(S.4)

where t is time and C is an arbitrary constant. After applying a weak field $\mathbf{a} = 0.034\hat{x}$ along the x-axis to relax the model, we change the field with $\beta = 60°$ angle difference and wait the director to rotate and align with the field (Fig. S.7). The results are fitted to Eq. S.4 using least-squares method with γ_1^* and C being two fitting parameters. Note that the relation between the viscosity and the order parameter is $\gamma_1^* \propto S^2$, we use the equilibrium order parameter $S \sim 0.7$ when measuring the viscosity. The result is $\gamma_1^* = 5.89$, which is in the same order of magnitude as reported in literature.[3]

7.2   A simple estimate of γ_1 and α_4

We also performed the viscous coefficient calculations using the quadratic dissipation function in the Ref[7], in which the authors used the quadratic dissipation function to describe the drag force acting on defects. Specifically, the force is the partial derivative of the dissipation function. The dissipation function at position $\mathbf{R}(t) = \big(X(t), Y(t)\big)$ with an orientation vector $\mathbf{p}(t) = \big(\cos \Psi(t), \sin \Psi(t)\big)$ can be written as follow[7]:

$$D = \frac{1}{2}D_1|\dot{\mathbf{R}}|^2 + \frac{1}{2}D_2(\mathbf{p} \cdot \dot{\mathbf{R}})^2 + \frac{1}{2}D_3|\dot{\mathbf{p}}|^2 + \frac{1}{2}D_4\dot{\mathbf{p}} \cdot \dot{\mathbf{R}},$$

where $D_{1,2,3,4}$ are coefficients corresponding to different dissipation modes.

For $+1/2$ defect, the macroscopic theory implies the dissipation function:

$$D = \frac{1}{2}D_1|\dot{\mathbf{R}}|^2 + \frac{1}{2}D_2(\mathbf{p} \cdot \dot{\mathbf{R}})^2 = \frac{1}{2}D_1\dot{x}^2 + \frac{1}{2}D_2\dot{x}^2 \cos^2 \Psi,$$

$$F_x^{\text{drag}} = (D_1 + D_2 \cos^2 \Psi)\dot{x}.$$

The authors use minimal model to integrate the dissipation function. And with the assumption that $\gamma_1/\alpha_4 \ll 1$, the dissipation coefficients of $+1/2$ defect D_1 is found as

$$D_1 = \frac{\pi\gamma_1}{4} \log \frac{r_{\text{max}}}{r_c} - \frac{\pi\gamma_1^{3/2}}{2^{7/2}\alpha_4^{1/2}} \left[\left(\log \frac{r_{\text{max}}}{r_c}\right)^2 + \left(\log \frac{r_{\text{max}}}{r_c}\right) - \frac{5}{2} \right],$$

where $r_{\max}$ is the system size and r_c is defect core size. Furthermore, we see that the dissipation function of integration does not depend on the defect orientation Ψ at all, and hence $D_2 = 0$.

For the $-1/2$ defect, the macroscopic theory implies the dissipation function:

$$D = \frac{1}{2} D_1'|\dot{\mathbf{R}}|^2 = \frac{1}{2} D_1' \dot{x}^2,$$

where the coefficient D_1' is

$$D_1' = \frac{\pi \gamma_1}{4} \log \frac{r_{\max}}{r_c} - \frac{\pi \gamma_1^{3/2}}{2^{7/2} \alpha_4^{1/2}} \left[\left(\log \frac{r_{\max}}{r_c} \right)^2 - 7 \left(\log \frac{r_{\max}}{r_c} \right) + \frac{11}{2} \right],$$

and the drag force is

$$F'^{\text{drag}}_x = D_1' \dot{x}.$$

In our simulation, we take the drag force equal to the elastic force, and consider their x-components. Therefore, we can combine $F = -\frac{\partial E_{\text{el}}}{\partial d} = -\frac{2\pi K^* k_1 k_2 L_z^*}{d^*}$ (elastic force in the main text) and the drag force mentioned above. To be consistent with the 2D case in the theory with our 3D system, we use $F^{\text{drag}}_x = \frac{F}{L_z^*}$, where L_z^* is the thickness in the z-dimension. Using the units in the main text, we find $\gamma_1^* = 3.11$, comparing to $\gamma_1^* = 5.89$ measured using the rotating field method, and $\alpha_4^* = 88.37$ comparing to $\alpha_4^* = 4.57$ reported in literature.[4] We note that the assumption of $\gamma_1 \ll \alpha_4$ is needed for this estimate to be accurate.

8 Size effect on elastic constant measurement

In the main text, we have estimated the elastic modulus by equating the elastic energy and the thermal energy in NVE ensemble. To examine the size effect on this estimation method, we used the equation $K^* = \frac{N k_B \Delta T^*}{2\pi k_1 k_2 L_z^* \ln \frac{d^*}{2r_c^*}}$ for a range of systems of different sizes in Fig. S.8.

The result, summarized in Table. 1, show that the estimated K^* fluctuates around 4 for $d^* \geq 36$ and becomes significantly large for $d^* = 18$. The estimate is sensitive to the defect core size r_c^*. When d^* and r_c^* are comparable, the estimate becomes inaccurate. For small systems, thermal fluctuations of temperature could also deteriorate the accuracy of the estimate.

Table 1 Elastic constant measured from the energy conservation law with different sizes.

N	d^*	K^*
$5,000$	18	9.29
$20,000$	36	3.65
$45,000$	54	5.21
$80,920$	61	3.66
$112,000$	70	4.61

9 Size effect on thermal fluctuations

The size effect of thermal fluctuations in different ensembles is studied in this section. In Fig. S.8, we measured the relative fluctuation of thermodynamic variable x, with $x = V$, P, and T for NPT, NVT, and NVE ensemble, respectively. The results show that the thermodynamic theory that relative fluctuation is proportional to $1/\sqrt{N}$ holds in our system.
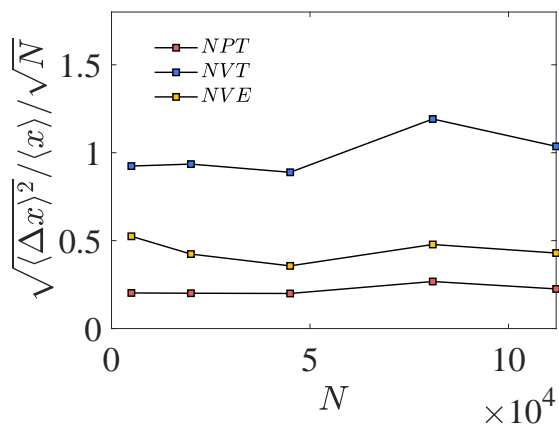

Figure S.8. Thermal fluctuations for different system sizes. $x = V$, P, and T for NPT, NVT, and NVE ensemble, respectively.

References

[1] Pierre-Gilles De Gennes and Jacques Prost. *The physics of liquid crystals*. Number 83. Oxford university press, 1993.

[2] Satoru Kuwajima and Atsutaka Manabe. Computing the rotational viscosity of nematic

liquid crystals by an atomistic molecular dynamics simulation. *Chemical Physics Letters*, 332(1-2):105–109, 2000.

[3] Geoffrey R Luckhurst and Katsuhiko Satoh. The director and molecular dynamics of the field-induced alignment of a gay–berne nematic phase: An isothermal-isobaric nonequilibrium molecular dynamics simulation study. *The Journal of Chemical Physics*, 132(18):184903, 2010.

[4] Katsuhiko Satoh. Thermodynamic scaling of miesowicz viscosity coefficients via molecular dynamics simulation. *Molecular Crystals and Liquid Crystals*, 615(1):78–88, 2015.

[5] N Schopohl and TJ Sluckin. Defect core structure in nematic liquid crystals. *Physical review letters*, 59(22):2582, 1987.

[6] Iain W Stewart. *The static and dynamic continuum theory of liquid crystals: a mathematical introduction*. Crc Press, 2019.

[7] Xingzhou Tang and Jonathan V Selinger. Theory of defect motion in 2d passive and active nematic liquid crystals. *Soft Matter*, 15(4):587–601, 2019.